Synthesis and characterization of electrospun nanofibers of Sr-La-Ce oxides as catalysts for the oxidative coupling of methane

Brenda M. Sollier, Magali Bonne, Nabyl Khenoussi, Laure Michelin, Eduardo Ernesto Miró, Leticia Ester Gómez, Alicia V. Boix, and Bénédicte Lebeau

Synthesis and characterization of electrospun nanofibers of Sr-La-Ce oxides as catalysts for the oxidative coupling of methane.

Brenda M. Sollier[a], Magali Bonne[b], Nabyl Khenoussi[c,d], Laure Michelin[b], Eduardo E. Miró[a], Leticia E. Gómez[a], Alicia V. Boix[a*], Bénédicte Lebeau[b]

a- Instituto de Investigaciones en Catálisis y Petroquímica, INCAPE (FIQ, UNL-CONICET), 3000 Santa Fe, Argentina.

b- Université de Haute Alsace (UHA), CNRS, IS2M UMR 7361, F-68100 Mulhouse, France

c- Université de Haute Alsace (UHA), LPMT, F-68100 Mulhouse, France

d- Université de Strasbourg, 4 rue Blaise Pascal CS 90032 F-67081 Strasbourg France.

*Corresponding autor:

Alicia V. Boix

INCAPE. Santiago del Estero 2829 (3000) Santa Fe Argentina

54 342 4536861

email: aboix@fiq.unl.edu.ar

1

Abstract

Catalytic nanofibers composed of La-Ce and Sr-La-Ce oxides were synthetized by electrospinning method with 5 wt.% of Sr and different La/Ce molar ratios. The materials were obtained by calcining electrospun polymer composite fibers and were studied for the oxidative coupling of methane (OCM). The catalytic performance was compared with analogous Sr-La-Ce powder catalysts.

SEM micrographs of Sr-La-Ce fibers (La/Ce: 0.1, 0.2, 1 and 3) showed nanostructures with homogenous and uniform diameters (170-200 nm). In addition, the XRD patterns revealed the formation of crystalline solid solutions like $La_xCe_yO_z$. The strontium enhanced the CH_4 conversion and C_2 selectivity, since it possibly generated structural defects that promote the formation of superoxide species. The SrLaCe3 nanofibers reached a CH_4 conversion of 28.5 % and C_2 yield of 21.7 % at 600 ºC. The nanofibers randomly packed improved the heat and mass transfer properties due to a high geometric surface ratio with high bed porosity.

Keywords: $La_xCe_yO_z$ solid solution; electrospinning technique; surface characterization; OCM; high C_2 yield.

2

1. Introduction

A large number of fibrous materials have been described in the literature and a significant part of these are in patent documents. In particular, fibrous catalysts offer flexibility and endless forms, which not apply to the usual powdered or granular materials. Comparison of fibers catalysts with powder and monoliths reveals that structured fibrous catalysts are versatile and may find many applications. Cloths made from fibers of easy handling can be packed to fit into almost any geometry.[1,2]

Furthermore, the use of catalytic materials with fibrous structure of micro-nanometric size may present several advantages with respect to powdered ones. They show low resistance to internal diffusion and high surface area to volume ratio because of their very small diameter. These fibrous structures combine less significant temperature gradients and lower pressure drop in a fixed bed reactor than those in powder form due to the high void fractions or bed porosity.[3]

On the other hand, electrospinning is a remarkably simple and powerful technique for generating continuous and thin fibers using a variety of different materials. For application in catalysis, one dimensional polymer fibers that result from electrospinning can be used as a template for synthesis of simple oxide or mixed oxides catalysts. In this process, polymer and inorganic precursors solutions are electrosprayed together to give a composite fiber containing the catalytic precursors which are eliminated with a posterior calcination process.[4]

Recently, nanostructured fiber-based catalysts have ever-increasing attention for the industrial catalysis and environment protection. Fiber-structured catalysts have been developed for a wide range of reactions, including diesel soot combustion[5], CO

3

Oxidation[4,6], CO oxidative coupling to DMO[7,8], alcohol selective oxidation[9,10], Fischer-Tropsch synthesis[11], dry reforming of CH_4[12,13] methanol to propylene[14], etc.

In the last decades, the direct and indirect methods to convert methane into more valuable products, including olefins and higher-molecular-weight hydrocarbons, have received great attention.[15,16] In this vein, oxidative coupling of methane (OCM) is an interesting approach, which holds great prospect in converting methane directly into higher hydrocarbons in the presence of oxygen.[17,18] The most common product obtained by OCM is ethylene, which is known as a vital chemical platform for synthesis of most petrochemical products.[19,20]

During the 90s, despite the research efforts devoted to the OCM reaction, no acceptable C_2 (ethane and ethylene) yield was accomplished to justify its industrial application. However, some significant conclusions were academically achieved about the reaction mechanism and active catalyst sites. In this way, methane dehydrogenation and methyl radical coupling were considered as the clue reaction steps.[21] In this way, acceptable reaction performances have been reached with oxides as MgO, MnO_2, and La_2O_3. These oxides could be promoted by basic compounds like Li, Na and Sr that can contribute to generate superficial active sites for methane dehydrogenation.[22–24] Early studies reported that La_2O_3 catalysts doping with Sr showed promising OCM activity because of their high C_2 yield and thermal stability.[22] Moreover, the CeO_2 is well known as a redox-active catalyst, which may help to diminish coke formation and thus improve the activity and durability of catalyst.[25]

However, most catalysts for the OCM were studied on its powder form, fixed-bed reactors randomly packed, which is not useful for industrial applications. Therefore, under industrial conditions, high flows should be used at relatively high temperature, structured

4

catalysts could be a good option, because they provide lower pressure drop, smaller diffusion resistance and better mass and heat transfer than powder catalysts.[26,27] Recently, we have reported promising results obtained with Sr-La_2O_3 coated onto ceramic monoliths and foams. Especially, interesting conclusions were obtained with Sr/La_2O_3 catalysts deposited on the walls of cordierite monoliths; an important increase in both, methane conversion and C_2 yield, took place. It has been found that monolithic structure provided physical and chemical beneficial effects. That is; the disposition of the catalyst on the straight channel allowed a more homogeneous flow which resulted in a better contact between reactant and catalyst surface and then, in an increase of the overall reaction rate. Moreover the catalytic layer enrichment with Mg and Si, coming from the cordierite structure, greatly contributed to the improved catalytic behavior.[28,29] On the other hand, nanofiber-structured catalysts based on CeO_2-La_2O_3[30,31] and Sr-La_2O_3[32] showed relevant catalytic behavior in OCM reaction.

Although the main criteria for industrial application of the OCM demanded that the catalysts were able to reach a C2 yield higher than 25 %,[33] some economical estimates demonstrated that the yields about 12%−15% could be sufficient for economically feasible production of ethylene via OCM in the areas where the relative cost of natural gas compared to ethylene is low enough.[34]

In this sense, the production of shale gas has been increasing year by year since new deposits distributed throughout the planet were discovered. Therefore, this fact encourages the production of these higher value products.

Thus, in this work catalysts based on Sr-La-Ce with nanofiber morphology for the oxidative coupling of methane were studied. Therefore, different systems of La-Ce and Sr-La-Ce nanofibers were synthesized by the electrospinning method and they were tested in

5

the catalytic reaction. The prepared solids were characterized by scanning electron microscopy (SEM) with Energy Dispersive X-Ray Spectroscopy (EDX), X-ray diffraction (XRD) and X-ray photoelectron spectroscopy (XPS). The La-Ce and Sr-La-Ce catalytic fibers were used for the oxidative coupling of methane (OCM) and the performances of the best catalytic fibers were compared to the conventional powder catalysts.

2. Experimental

2.1 Materials and methods

2.1.1 Precursor materials

Cerium nitrate hexahydrate $(Ce(NO_3)_3.6H_2O$, Sigma Aldrich), lanthanum nitrate hexahydrate $La(NO_3)_3.6H_2O$ (Sigma Aldrich), strontium nitrate $Sr(NO_3)_2$ (Sigma Aldrich), poly(vinylpyrrolidone) (PVP M_w 360,000, Sigma Aldrich), ethanol (Sigma Aldrich), citric acid and distilled water were used without further purification.

2.1.2 Nanofiber catalysts preparation

Two series of nanostructured catalysts were prepared with different concentrations, one composed of La and Ce (labeled LaCex), and the other composed of La, Ce and Sr (labeled SrLaCex) where x means La/Ce molar ratio. The fibers were prepared with an Elmarco's Nanospider (NS 1WS500U series), a wire-electrode needleless electrospinning system. To prepare the electrospinning solution, 1.16 g of salts were weighted and were dissolved in a mixture of 40 mL ethanol and 8 mL water. The amount of each precursor salt was determined in order to obtain the theoretical compositions (molar ratios La/Ce: 0.1,

6

0.2, 1 and 3) with or without 5 wt.% of Sr. This mixture was maintained under continuous stirring at room temperature for 15 min. Then, 4 g PVP was added and the resulting mixture was kept overnight under continuous stirring at room temperature. The prepared solutions were introduced into the machine injector. Firstly, the parameters of the electrospinner were optimized in order to obtain well-formed nanofibers. Pumps were set at different air flows: 30-20, 50-40, 60-50, 70-60 $m^3 h^{-1}$, and two voltages were also tested at 30 and 40 kV. The temperature and humidity were set at room conditions. Electrospun fibers were calcined at 625 ºC in a furnace for 10 hours with a heating ramp of 0.5 ºC min^{-1}. The calcination temperature was determined by means of TG analysis, proving that at 625 ºC all PVP is decomposed. The BET area (specific surface area) of nanofibers was very low, (10-15 $m^2 g^{-1}$) which indicates that these are dense and do not have internal porosity.

2.1.3 Powder catalysts preparation

Some powder catalysts were prepared in order to compare their catalytic performance to nanofibers. La-Ce mixed oxide was synthesized from $Ce(NO_3)_3 \cdot 6H_2O$ and $La(NO_3)_3 \cdot 6H_2O$ by the citrate method. The proper amounts of precursors were weighted in order to obtain a La:Ce molar ratio of 3. These precursors were dissolved in water and citric acid was added in a molar ratio of acid/(Ce+La) = 1. The final solution was heated up to 80 ºC under constant stirring to evaporate superfluous water until a viscous gel was obtained, which was dried at 120 ºC for 24 h to form a spongy material. Finally, this material was calcined at 625 ºC for 6 h and it was named as LaCe3-powder.

On the other hand, Sr was added to LaCe3-powder by wet impregnation in the proper amounts to obtain 5 wt.% of strontium. $Sr(NO_3)_2$ was dissolved in water and LaCe3-powder

was added to the solution. The mixture was kept under continuous stirring at 80 ºC for 4 h. Then, it was dried in an oven at 120 ºC overnight and it was calcined at 625 ºC for 6 h. Finally, this sample was called SrLaCe3-powder. The BET areas (specific surface area) were 9.8 and 9.3 m^{2}g^{-1}, which suggests that they are non-porous materials.

2.2 Characterization techniques

The obtained fibers were analyzed using scanning electron microscopes (JEOL JSM-IT100 or Philips XL30). Both were equipped with an EDX analyzer. The samples were first gold-coated using a sputter coater. The mean diameter was measured using image analysis software (Image J) from 100 fibers.

X-Ray diffraction patterns were collected on a PANalytical MPD X'Pert Pro diffractometer operating with Cu K$_\alpha$ radiation (K$_\alpha$=0.15418 nm) equipped with an X'Celerator real-time multiple strip detector (active length=2.12°2θ). The powder patterns were collected at 25 °C in the range 3<2θ<70, step= 0.017°2θ, time/step=220s. The phases identification has been measured with the X'Pert High score software (PANalytical) and the PDF-4+ 2018 database from the International Centre for Diffraction Data (ICDD).

X Ray photoelectron analysis (XPS) was performed in a multi-technique system (SPECS) equipped with a dual Mg/Al X-ray source and a hemispherical PHOIBOS 150 analyzer operating in the fixed analyzer transmission (FAT) mode. The spectra were obtained with a pass energy of 30 eV, the Al Kα X-ray source (hυ = 1486.6 eV) was operated at 200 W and 12 kV. The working pressure in the analyzing chamber was less than $2 \cdot 10^{-6}$ Pa. Casa XPS software was employed for data treatment corresponding to

8

regions O 1s, C 1s, Sr 3d, La 3d and Ce 3d (as internal reference u''' 916.5 eV). Peaks were considered as a mixture of Gaussian and Lorentzian functions in a 70/30 ratio.

2.3 Catalytic tests

The experiments were conducted in a fixed-bed flow quartz reactor at atmospheric pressure. The reactor design was described in a previous work.[29] The reactant flow entered the reactor through an inner section of 16 mm diameter, but below the catalytic bed this inner section was reduced up to 1/8 inch diameter in order to decrease the homogeneous combustion of hydrocarbon products as much as possible.

The system was heated with a furnace to reach the desired temperatures. The exiting gases from the reactor were conducted through a condenser in order to remove H_2O from the flow. Finally, the exiting flow concentrations were measured using a gas chromatograph (GC-2014 Shimadzu) with thermal conductivity detector (TCD) equipped with two columns, zeolite 5A and Hayesep D. The carbon balance was always higher than 97 %. The catalytic tests were repeated several times over the samples, showing quite reproducible results.

The catalytic nanofibers (250 mg) were loosely packed into a 16 mm (inner diameter) quartz tube between two quartz wool plugs. The bulk density of catalytic bed was approximately 0.06 g cm^{-3}. For comparison, powdered catalysts (500 mg) were evaluated; they had a bulk density around 0.5 g cm^{-3}.

The reaction mixture consisted of 60 vol.% CH_4, 12 vol.% O_2 and 28 vol.% He. The gas flow rates were adjusted by means of controllers in order to achieve catalyst-

9

weight/total flow ratio = 0.166 mg cm^{-3} h. The catalysts were tested in a wide temperature range (250-700 °C). Methane conversion, C2 selectivity and C2 yield were calculated as follows:

$$Methane\ conversion, X_{CH_4}(\%) = \frac{Molar\ flow\ of\ CH_4\ reacted}{Molar\ flow\ of\ CH_4\ in\ feed} \times 100$$

$$C2\ Selectivity, S_{C2}(\%) = 2\frac{Molar\ flow\ of\ C2}{Molar\ flow\ of\ CH_4\ reacted} \times 100$$

$$C2\ Yield, Y_{C2}(\%) = Methane\ conversion \times C2\ Selectivity\ \times \frac{1}{100}$$

Being C2 ethane and/or ethylene.

3. Results and Discussion

3.1. Characterization of catalytic nanofibers

The theoretical compositions of the catalytic nanofibers La-Ce and Sr-La-Ce obtained by electrospinning are detailed in Table 1. The La/Ce molar ratios were 0.1, 0.2, 1 and 3 and the Sr content was 5 wt.% in all samples.

In order to select the best operating conditions for the formation of nanofibers from the precursor solutions, the parameters in the electrospinning machine were varied. The morphology of the obtained nanofibers was studied by SEM. Micrographs taken from the LaCe3 samples (before calcination) obtained with different electrospinning machine parameters are shown in Figure 1.

Two parameters were varied; air flux and voltage, and seven different samples were obtained. The lowest and highest flux (30 - 20 and 70 - 60 m^3 h^{-1}, respectively) did not

show good results (Fig 1 (A), (D) and (G)), no nanofibers were obtained. This behavior was observed with both applied voltages (30 and 40 kV). It seems that some nanofibers were obtained with 60 - 50 m^3 h^{-1} under 40 kV, but the sample was heterogeneous and some agglomerations could be seen in Figure 1(F). The sample obtained with this air flux value, but under 30 kV was not composed of nanofibers (Fig. 1(C)). Finally, with the air flux value of 50 - 40 m^3 h^{-1} and a voltage of 30 kV, homogeneous nanofibers of LaCe3 sample were obtained (Fig. 1(B)). These latter parameters, 50 - 40 m^3 h^{-1} and 30 kV, were selected to prepare the samples that were studied in this work.

The SEM micrographs of the nanofibers obtained only with the polymer (PVP), the Ce and La salts and PVP (LaCe0.1@PVP) before and after calcination (LaCe0.1) are depicted in Figure 2.

The image of the obtained nanofibers from the PVP polymer is shown in Fig. 2(A). In this case, the fibers diameters are the largest in this studied set with an average diameter of 500 nm, including one that reaches 1.05 μm. When the salts were added into the electrospinning solution, the average nanofiber diameter decreased, being of around 400 nm (Fig. 2(B)). This decrease could be related to the fact that the addition of salts to the electrospinning solution increases conductivity, improving the spinning procedure. Finally, when the LaCe0.1 nanofibers were calcined, the diameters decreased again, reaching values of around 150 nm (Fig. 2(C)). This phenomenon is caused by the polymer removal from the nanostructures, and also by the formation of the mixed oxides (La_xO_y-Ce_zO_t).

In addition, SEM micrographs of four LaCe compositions (after calcination at 625°C) are depicted in Figure 3. In these samples (A-D) the nanostructures could be seen. The

11

samples are homogeneous and uniform. In Figure 3(E) - (G) micrographs at higher magnifications are displayed. In LaCe0.1 SEM micrograph (Fig. 3(E)) it seems that thin nanofibers, of around 140 nm diameter, are attached each other forming a fiber of larger diameter, between 350 and 450 nm. The same phenomenon is observed in LaCe0.2 (Fig. 3(F)). LaCe3 sample was somewhat different, the nanofibers are not all of them glued and thin nanofibers of around 200 nm diameter are observed (Fig. 3(G)). However, there is one big fiber in the middle of the picture for which this phenomenon of nanofibers packing is observed.

Figure 4 shows the SEM micrographs of SrLaCe nanofibers (after calcination at 625°C) from four samples with different compositions. In the first four images (Fig. 4A-D) it could be seen that the nanostructures are homogeneous and uniform. In SrLaCe0.1 micrographs (Fig. 4A and E) shorter nanofibers are observed, indicating that somehow the addition of Sr to the solution contributes to shorten nanostructures. This phenomenon was not observed in the other three samples. In SrLaCe3 the diameter of the fibers was measured and values of around 171 nm were obtained (Fig. 4(F)). This diameter was lower than those of LaCe3, suggesting that the addition of Sr to the electrospinning solution increases its conductivity, improving the experiment conditions and lowering nanofibers diameters. The same average diameter of about 150 nm was observed for the other three samples (Fig. 4 (F) - (H)).

The atomic concentrations of the different elements determined by EDX analyses in SrLaCe0.1, SrLaCe0.2, SrLaCe1 and SrLaCe3 samples are reported in Table 2. The sample SrLaCe0.1 exhibits a La and Ce values of 1.9 and 16.0 %, respectively, which results in La/Ce ratio of 0.11, similar to the theoretical one (see Table 1). The oxygen concentration

12

(57.2 %) corresponds to the formation of oxides, hydroxides and/or carbonates. The presence of C could be due to carbonates formation in the samples that will be discussed in the next sections. All samples showed similar Sr concentration (around 4.5-4.7%), which indicates a homogeneous dispersion of Sr in nanofibers. Also, the La/Ce ratios resulted in 0.26, 1.07 and 3.18 for SrLaCe0.2, SrLaCe1 and SrLaCe3, respectively, in agreement with the theoretical ones. These results suggest that during synthesis, there is no preferential deposition of any component onto the collector film. Additionally, in the Figure S1 (supporting information) SEM-EDX results and elements spectra measured for SrLaCe3 nanofibers are shown.

On the other hand, SEM image and EDX result for LaCe3 are shown in the Figure S2 (Supporting Information). The formation of very irregularly shaped large particles can be observed in calcined LaCe3 powder.

Figure 5 shows the XRD patterns of four LaCe samples with the positions of the characteristic crystalline CeO_2 diffraction peaks (at 28.56, 33.08, 47.48 and 56.34°2θ, full line) and La_2O_3 diffraction peaks (at 27.02, 31.31, 44.86 and 53.16°2θ, dot line).[35] It can be noted that if the pattern of LaCe0.1 is very close to the pattern of CeO_2 the higher the percentages of lanthanum incorporated are, the more shifted to the La_2O_3 peak positions the patterns are. These displacements correspond to the formation of solid solutions with $La_xCe_yO_z$ formula (with x and y linked to the peak shifts) and have been confirmed by the identification of the phases found and presented in the Table 1. This identification is in good agreement with the theoretical ratios La/Ce and the ratios of the solid solution compositions obtained by XRD, which seems to indicate that the lanthanum is well incorporated in the CeO_2 structure. However, the LaCe3 patterns show the presence of

13

additional small quantities of crystalline CeO_2. The XRD results are in good agreement with those of Noon and co-workers[30] for La_2O_3-CeO_2 nanofibers. They established that in their samples, solid solutions were formed by reactions between La_2O_3 and CeO_2, such as the partial reduction of ceria into Ce_7O_{12} and the incorporation of La^{3+} ions into the cubic lattice of CeO_2.[36,37] From XRD patterns, it was estimated the crystallite sizes by means of Scherrer equation for each La-Ce samples. The main diffraction CeO_2 signal was used to calculate the size and the obtained values were around 10 and 11 nm.

The SrLaCe XRD patterns are shown in Figure 6. The results are quite similar to those obtained for LaCe samples and give also solid solutions. Nevertheless, in all the patterns, some new XRD peaks appear at 25.34, 25.90, 35.35, 36.78 and 44.11° 2θ, which correspond to $SrCO_3$ crystalline phase.[38] The SrLaCe0.1 pattern is a little more left shifted than the LaCe0.1 XRD pattern. This pattern identification does not permit to give an exact solid solution composition. As mentioned in the Table 1, several ICDD reference cards could be attributed to this XRD pattern: variable solid compositions (% of lanthanum ranges from 0.05 to 0.15) could correspond as well an ICDD card (04-021-0597), which contains strontium insertion in the solid solution. For this XRD pattern and the others it is not possible to conclude by XRD if the strontium is well inserted in the solid solutions or just present as crystalline $SrCO_3$. No significant differences are observed in the SrLaCe0.2 XRD pattern compared to the one of LaCe0.2, only the presence of peaks characteristic of $SrCO_3$ was observed. For higher lanthanum concentration, it seems that the presence of strontium changes the solid solutions formed. For SrLaCe1, two solid solution compositions can be distinguished and for SrLaCe3, the pattern shows less incorporation of lanthanum in the solid solution than in the LaCe3 (left shift lower than this of LaCe3).

14

On the other hand, XRD patterns of LaCe3-powder and SrLaCe3-powder shown no significant differences compared to LaCe3 and SrLaCe3 nanofibers. This fact suggests that the crystalline phases developed during the calcination stage at 625 ºC are similar in powders and nanofibers (See Figure S3 in Supporting Information).

The XPS results from LaCe3 and SrLaCe3 catalysts are shown in Table 3. Both of them were previously used in the OCM reaction. The La 3d doublet is well defined showing the satellite structure appearing on the high side of $3d_{5/2}$ and $3d_{3/2}$ peaks. In LaCe3, the La $3d_{5/2}$ core level is at 835.6 eV and its corresponding satellite at +4.0 eV (see Fig. 7(A)). According to literature, both lanthanum species, La_2O_3 and $La(OH)_3$, have close binding energies (BEs) positions.[39,40] Sunding et al.[41] reported La $3d_{5/2}$ values of 835.0 eV for La_2O_3 and 835.1 eV for $La(OH)_3$. In our catalyst, LaCe3, the La ($3d_{5/2}$-$3d_{.3/2}$) doublet show higher values, suggesting that different chemical environment around La exist (Table 3). This is related to the XRD analysis, which suggested that La-Ce forms mixed oxides. In addition, the incorporation of Sr to the catalytic system slightly decreases BEs of satellites and main peaks.

The complex Ce 3d spectrum of LaCe3 catalyst was fitted with six component peaks (denominated v, v'' and v''' for Ce $3d_{5/2}$ and u, u'' and u''' for Ce $3d_{3/2}$) whose BEs positions were very close to those found for the CeO_2 (Ce^{4+}). The Ce $3d_{5/2}$ BEs in LaCe3 were 882.9, 888.4, 898.1 eV. According to Paparazzo et al.[42], these energies are associated to Ce^{4+} species. This behavior is in agreement with the sample pre-treatments: calcination under air at 625 ºC and the exposure to reaction in oxidizing conditions. The Sr incorporation to the system does not show significant differences in Ce 3d binding energy positions.

15

On the other hand, in O 1s region three peaks appeared at 529.1, 530.6 and 533.2 eV over LaCe3 catalytic fibers (see Fig. 7(B)). The peak at lower binding energy corresponds to lattice oxygen (O^{2-}) which represents 8.9 % of the total amount of oxygen. Whereas the one at 530.6 eV could be attributed to a mixture of different species, including hydroxyl (OH^-), carbonate (CO_3^{2-}) and peroxide ion (O^-), all with similar BEs according to literature. This signal represents 44.8 % of total oxygen. The carbonate and hydroxide species could have been formed on the fiber surface by contact with atmosphere air. The carbonate species were seen also in C 1s region, with a signal around 291 eV. The latter oxygen peak, at 533.2 eV, is the main signal, with a concentration of 46.3 %. In our previous work, this peak was identified as the superoxide species (O_2^-).[28,29] Islam et al.[43] investigated the formation of peroxide and superoxide species on Sr-La catalysts. It was reported that electron deficient species, such as O^- and O_2^-, on the catalytic surface, are helpful to increase methane molecule activation during OCM reaction.[32,44] In SrLaCe3 catalytic fibers, the superoxide concentration is significantly higher than in LaCe3. It represents around the 64 % of total oxygen, this suggests that the incorporation of Sr to the catalytic system increases the amount of active species in SrLaCe3. This latter fact will be discussed in the next section.

In SrLaCe3 it was also analyzed Sr 3d region and two components were detected at 134.8 and 136.6 eV, the spectrum was introduced in Figure 7(C). The signal at lower binding energy corresponds to SrO and it represents the 63.6 % of Sr, as it is shown in Table 3. The signal that appears at 136.6 eV corresponds to $SrCO_3$ and it is the 36.6 % of total strontium.[32,45] Nevertheless, these values are at higher BEs than usual (132.1 and 133.9 eV for SrO and $SrCO_3$ respectively).[46] J. Kuyyalil et al.[47], attributed this shift to the

strontium electrochemical environment. They concluded that this phenomenon could be due to the interaction of Sr with the oxygen vacancies.

Table 4 shows the surface atomic concentrations calculated from the XPS data of LaCe3 and SrLaCe3. These values show the composition of surface layers with a depth of 20-40 Å, where the La/Ce atomic ratio greater than 3, suggests an enrichment of the surface in lanthanum.

3.2. Catalytic performance

Methane conversion versus temperature for LaCe3, LaCe1 and LaCe0.2 nanofibers is shown in Figure 8 (A). It can be observed that the conversion values increase with the temperature to achieve maximum values of 24.6 and 14.1 % at 600 ºC for LaCe3 and LaCe0.2, respectively, while LaCe1 reaches 20.3 % at 550 ºC. Selectivity towards C_2 (Fig. 8 (B)) increases with temperature. LaCe3 shows mostly uniform values from 350 to 550 ºC, these values raise from 34.4 to 40.3 %. At 600 ºC, it is observed 62.4 % of C_2 selectivity. The LaCe1 nanofibers showed similar behavior, reaching 54.2 % at 600 ºC, while LaCe0.2 selectivity was null at 350 - 400 ºC and it started to increase at 450 until 600 ºC, with a maximum value of 40.1 %. In Figure 8(C) the C_2 yield of LaCe nanofibers is shown, as the temperature increases the C_2 yield increases, with maximum values at 600 ºC: 15.4% for LaCe3, 10.3% for LaCe1 and 5.6% for LaCe0.2. This behavior clearly shows that the lanthanum concentration in the catalyst is key for OCM reaction. The more La concentration in the catalyst is, the better the reaction performance is. To study the nanostructure influence in OCM, it is also included in Figure 8(C) C_2 yield of LaCe3-powder to compare with the LaCe3 nanofibers. It could be observed that in the powder

approximately the same maximum was achieved (~15%) but at a higher temperature, 750 ºC. This is suggesting that the nanostructure is improving the reaction conditions; particularly it is beneficial to lower the working reaction temperature. The differences in surface area and the dispersion of the elements could be also in part responsible for this improvement.

In Figure 9 it is introduced the catalytic performances of SrLaCe nanofibers. Figure 9(A) shows the methane conversion increasing with temperature for the four different catalysts. The best catalytic performance was observed with SrLaCe3 nanofiber, where methane conversion is 10.6 % at 350 ºC, and this value augments smoothly to 13.6 % until 500 ºC. At 600 ºC, it increases notably to 28.5 %. To assess the performance at higher temperatures, this catalyst was also tested at 700 ºC, and the conversion stayed mostly stable. The same behavior was observed for SrLaCe1, but the conversion was lower, it reached a maximum of 19.1 % at 600 ºC. For SrLaCe0.2 and SrLaCe0.1 the methane conversion values were lower. In Figure 9(B) it is shown selectivity towards C_2 of SrLaCe nanofibers. SrLaCe0.2 and SrLaCe0.1 selectivities increase with temperature to reach 39.3 and 33.5 % at 600 ºC, respectively. The selectivity of SrLaCe3 varies from 77 to 80 % between 350 and 500 ºC. From 500 ºC it decays until 70 % at 700 ºC. Although, for SrLaCe1, C_2 selectivity had an upward trend from 47.7 (350 ºC) to 59.6 % (600 ºC). Figure 9(C) introduces the C_2 yield of the different SrLaCe catalysts. The catalysts with low lanthanum concentration, SrLaCe0.1 and SrLaCe0.2, showed a C_2 yield around 5 %. As it was mentioned before, the high concentration of cerium is detrimental for the catalytic activity. Ceria could be lowering the basic character of the catalysts and promoting C_2 hydrocarbon further oxidation. When lanthanum and cerium contents are equal, the

catalytic performance improves, a C_2 yield of 11.6 % was achieved at 600 ºC. Finally, the best catalytic activity was exhibited by SrLaCe3. The C_2 yield increases with temperature, reaching its maximum of 21.7 % at 600 ºC. This follows the same tendency that for the LaCe nanofibers. The catalyst with higher concentration of La shows the best behavior in OCM reaction. Moreover, if the results of LaCe3 and SrLaCe3 are compared, it could be clearly seen that the addition of Sr to the nanofiber improves the catalytic performance.

In addition, these catalytic results were better than those reported in our previous works, where monolithic Sr/La_2O_3 catalysts reached a C2 yield of 18 % at 800 °C on OCM reaction. The composition of the fibers arranged in a controlled structure are able to achieve higher C2 yields at lower temperatures. Table TS1 in Supporting information section shows a comparison of catalytic activity of La_2O_3-based catalysts under the form of different structures; powder, monoliths and nanofibers. It could be observed that the yield to C2 products rises when the catalysts was deposited on a monolithic structure with respect to a Sr/Al_2O_3 powder. On the other hand, when a low percentage of CeO_2 (atomic ratio La/Ce=3) was added to Sr/Al_2O_3 powder it reached higher C2 yield and a lower temperature (750 °C) than the others (800 °C). Even more, when the Sr-La-Ce catalysts were made by electrospinning as nanofiber structures, the highest C2 yield was obtained (21.7 %) and at temperature considerably lower (600 °C).

According to XPS results, the catalytic surface of SrLaCe3 had higher concentration of superoxides species (~ 64 %) than LaCe3 (~ 46 %). As it was mentioned before, it is believed that oxygen species that have an electron deficiency, as O_2^- and O^-, are the active sites in OCM reaction.[43] Moreover, the Sr incorporation into the catalyst was highly studied in this process.[48–50] It is known that the insertion of strontium into the lattice of the host

19

oxides affects its defect structure, and causes the formation of oxygen-anion vacancies.[51,52] These lattice defects are supposed to play an important role in the OCM and they are related to the superoxide and peroxide species.

Some other tests were performed over SrLaCe3 in order to understand the behavior observed between 350 and 500 ºC where C_2 yield raised smoothly and then jumped surprisingly at 550 ºC. The run was repeated and the catalytic measurements were performed while increasing temperature and after that, decreasing it. In the second case, only slightly higher C_2 yield values were obtained between 600 and 450 ºC. The described results can be interpreted on the light of the mechanism proposed by Karakaya et al.[25] In their study of OCM reaction mechanism over La_2O_3/CeO_2 nanofibers, they suggest that both gas-phase and surface reactions play significant roles for CH_4 activation, as well as C_2 and CO_x formation. Despite differences in the active catalytic sites for particular catalysts, it is generally known that the methane activation proceeds via the $CH_3^\bullet$ radical. The initiating $CH_3^\bullet$ formation reactions control the overall reaction rate. They propose two contributions to the heterogeneous pathway. One is the reaction of methane with surface-adsorbed oxygen.[53] This step is promoted by the oxygen vacancies that are produced because of the introduction of some elements into the catalysts oxygen lattice, creating defects. That could be the case of Sr, as it was discussed in the previous paragraphs. This phenomenon may be the one that is prevailing at low temperature (between 400 - 500 ºC). The second heterogeneous contribution for the methane activation can also be accomplished by reacting CH_4 with $OH^\bullet$ radicals due to the O-H bonds in H_2O (497 kJ mol^{-1}) are stronger than the C-H bond in CH_4 (439 kJ mol^{-1}).[54,55] These radicals can be found onto the catalytic surface, and they prevail at higher temperatures. Therefore, this could be the cause of the strong

increase in C_2 yield observed from 550 to 600 ºC. There exist some other reactions in the gas-phase chemistry that contributes to $CH_3^{\bullet}$ formation via both, oxidative and non-oxidative reactions which are generally known from combustion research.[55,56] However, this latter gas-phase chemistry route has less effect in OCM reaction than the heterogeneous pathway. The catalytic test shown in Figure 9, in which we study the reaction behavior increasing and decreasing temperature, indicated no deactivation of the catalyst in 40 hours of time-on-stream.

In addition, SrLaCe3-powder was prepared in order to compare with the nanostructured fibers. It is clearly shown in Figure 9(C) that the powder exhibits worse C_2 yields than the nanofibers. Moreover, the maximum yield of 19.5 % was reached at 750 ºC. Once more, the nanostructure is beneficial and it highly improves C_2 yield in OCM reaction. As said before, no only the morphology of the fibers is important in determining in improving C_2, the influence of the surface properties and the dispersion of the elements should not ruled out. Finally, it is demonstrated that the nanofiber structure allows the catalytic system to reach the maximum yields at lower temperatures, 150 ºC less. This phenomenon was already seen by other authors, and it could be ascribed to higher mass transfer properties of nanofiber catalysts as compared with the powder ones.[57]. Another important feature of nanofibers is the high aspect ratio, which gives rise to randomly packed beds with a much higher porosity.[4] The combination of a relatively high geometric surface area with high bed porosity would favour the methane dehydrogenation step, which is the rate-limiting one, and the release of methyl radicals to the gas phase, where they can be coupled to form ethane and ethylene. This could be a suitable explanation for the better performance of the nanofibers as compared to their powder form.

21

Another important factor that should be considered is the temperature profile inside the reactor. Due to OCM is a strongly exothermic reaction, the possible formation of hot spots with temperatures higher than those measured must be considered. However, we concluded that due to the low reactant flow and concentrations used in the experiments the heat flux calculated from the reaction enthalpy and the observed methane conversion is low (2.12 W). Therefore, the formation of important hot spots inside the reactor, not detected by the thermocouple, it is not expected. However, this is an important point to be taken into account, and requires further analysis, for example using a theoretical model to predict radial and axial temperature profiles. A thorough study about this point has been recently reported.[58]

The C_2 yield of SrLaCe3 is between the highest values reported in the literature at this temperature. It is believed that the tri-component catalysts show the best performances in OCM.[24] Notably, Othman et al. reported that an OCM reaction conducted in a novel microreactor composed of a hollow fiber membrane (made of $La_{0.6}Sr_{0.4}Co_{0.2}Fe_{0.8}O_{3-\delta}$ (LSCF)) led to an excellent C_2 yield of 39 % (highest reported so far in literature) at an approximate methane conversion of 50 %.[59] However, these results were obtained at 900ºC.

4. Conclusions

In summary, the addition of 5 wt.% of Sr to La_2O_3-CeO_2 nanofibers enhances the CH_4 conversion and C_2 selectivity, specially for SrLaCe3 and SrLaCe1. The catalyst with higher concentration of lanthanum shows the best behavior in OCM reaction. The addition of Sr promotes the formation of electron deficient oxygen species (as O^{2-} and O^-) on the catalytic surface which constitute active sites in the oxidative coupling of methane reaction.

The synergistic effects from combinations of each component in Sr-La-Ce nanofibers brought about an improved catalytic behavior for the OCM reaction carried out at lower temperature, which cannot be achieved over the conventional SrLaCe powder catalysts.

In the LaCe and SrLaCe nanofibers as well as in LaCe3 and SrLaCe3 powders, the formation of crystalline solid solutions with $La_xCe_yO_z$ formula were detected by XRD, in agreement with theoretical ratios La/Ce, where the lanthanum was well incorporated in the CeO_2 structure.

For SrLaCe3 nanofibers CH_4 conversion and C_2 yield were up to 28.5 % and 21.7 % at 600 ºC, respectively; while SrLaCe3-powder achieves C_2 yield of 19 % at 750 ºC. This behavior was ascribed to higher heat and mass transfer properties of catalytic nanofibers as compared with powder one. In addition, the combination of a relatively high geometric surface area with high bed porosity of nanofibers improves the catalytic performance on OCM reaction.

Conflict of interest

There are not conflicts to declare.

Acknowledgement

References

(1)   Thenmozhi, S.; Dharmaraj, N.; Kadirvelu, K.; Kim, H. Y. Electrospun nanofibers: New generation materials for advanced applications. *Mater. Sci. Eng. B Solid-State Mater. Adv. Technol.* **2017**, *217*, 36–48.

(2)   Matatov-Meytal, Y.; Sheintuch, M. Catalytic fibers and cloths. *Appl. Catal. A Gen.* **2002**, *231*, 1–16.

(3)   Ternero-Hidalgo, J. J.; Torres-Liñán, J.; Guerrero-Pérez, M. O.; Rodríguez-Mirasol, J.; Cordero, T. Electrospun Vanadium Oxide based submicron diameter fiber catalysts. Part I: Preparation procedure and propane ODH application. *Catal. Today* **2019**, *325*, 131–143.

(4)   Moreno, I.; Navascues, N.; Irusta, S.; Santamaria, J. Electrospun Au/CeO$_2$ Nanofibers: A highly accessible low-pressure drop catalyst for preferential CO oxidation. *J. Catal.* **2015**, *329*, 479–489.

(5)   Stegmayer, M. Á.; Milt, V. G.; Navascues, N.; Gamez, E.; Irusta, S.; Miró, E. E. Cobalt deposited on micro and nanometric structures of ceria and irconia applied in diesel soot combustion. *Mol. Catal.* **2020**, *481*, 100636.

(6)   Tao, L.; Zhao, G.; Chen, P.; Zhang, Z.; Liu, Y.; Lu, Y. Thin-felt mcrofibrous-structured Au-α-Fe$_2$O$_3$/ns-γ-Al$_2$O$_3$/Al-fiber catalyst for high-throughput CO oxidation. *Appl. Catal. A Gen.* **2018**, *556*, 180–190.

(7)   Wang, C.; Han, L.; Chen, P.; Zhao, G.; Liu, Y.; Lu, Y. High-performance, low Pd-

loading microfibrous-structured Al-Fiber@ns-AlOOH@Pd catalyst for CO coupling

to dimethyl oxalate. *J. Catal.* **2016**, *337*, 145–156.

(8)   Wang, C.; Ding, J.; Zhao, G.; Deng, T.; Liu, Y.; Lu, Y. microfibrous-structured

Pd/AlOOH/Al-Fiber for CO coupling to dimethyl oxalate: effect of morphology of

AlOOH nanosheet endogenously grown on Al-fiber. *ACS Appl. Mater. Interfaces*

2017, *9*, 9795–9804.

(9)   Zhao, G.; Deng, M.; Jiang, Y.; Hu, H.; Huang, J.; Lu, Y. Microstructured Au/Ni-

fiber catalyst: galvanic reaction preparation and catalytic performance for low-

temperature gas-phase alcohol oxidation. *J. Catal.* **2013**, *301*, 46–53.

(10)   Zhang, Q.; Li, Y.; Zhang, L.; Chen, L.; Liu, Y.; Lu, Y. Thin-Sheet Microfibrous-

Structured Nanoporous Gold/Al Fiber Catalysts for Oxidative Coupling of Methanol

to Methyl Formate. *J. Catal.* **2014**, *317*, 54–61.

(11)   Han, L.; Wang, C.; Ding, J.; Zhao, G.; Liu, Y.; Lu, Y. Microfibrous-structured Al-

fiber@ns-Al$_2$O$_3$ core-shell composite functionalized by Fe-Mn-K via surface

impregnation combustion: as-Burnt catalysts for synthesis of light olefins from

syngas. *RSC Adv.* **2016**, *6*, 9743–9752.

(12)   Chai, R.; Fan, S.; Zhang, Z.; Chen, P.; Zhao, G.; Liu, Y.; Lu, Y. Free-standing NiO-

MgO-Al$_2$O$_3$ nanosheets derived from layered double hydroxides grown onto

FeCrAl-Fiber as structured catalysts for dry reforming of methane. *ACS Sustain.*

Chem. Eng. **2017**, *5*, 4517–4522.

(13)   Chen, W.; Sheng, W.; Cao, F.; Lu, Y. Microfibrous entrapment of Ni/Al$_2$O$_3$ for dry

reforming of methane: Heat/mass transfer enhancement towards carbon resistance and conversion promotion. *Int. J. Hydrogen Energy* **2012**, *37*, 18021–18030.

(14)   Wang, X.; Wen, M.; Wang, C.; Ding, J.; Sun, Y.; Liu, Y.; Lu, Y. Microstructured fiber@HZSM-5 core-shell catalysts with dramatic selectivity and stability improvement for the methanol-to-propylene process. *Chem. Commun.* **2014**, *50*, 6343–6345.

(15)   Lunsford, J. H. Catalytic conversion of methane to more useful chemicals and fuels: A challenge for the 21st Century. *Catal. Today* **2000**, *63*, 165–174.

(16)   Schwach, P.; Pan, X.; Bao, X. Direct Conversion of methane to value-added chemicals over heterogeneous catalysts: challenges and prospects. *Chem. Rev.* **2017**, *117* , 8497–8520.

(17)   Kondratenko, E. V.; Peppel, T.; Seeburg, D.; Kondratenko, V. A.; Kalevaru, N.; Martin, A.; Wohlrab, S. Methane conversion into different hydrocarbons or oxygenates: Current status and future perspectives in catalyst development and reactor operation. *Catal. Sci. Technol.* **2017**, *7*, 366–381.

(18)   Olivos-Suarez, A. I.; Szécsényi, À.; Hensen, E. J. M.; Ruiz-Martinez, J.; Pidko, E. A.; Gascon, J. Strategies for the direct catalytic valorization of methane using heterogeneous catalysis: challenges and opportunities. *ACS Catal.* **2016**, *6*, 2965–2981.

(19)   Galadima, A.; Muraza, O., Revisiting the oxidative coupling of methane to ethylene in the golden period of shale Gas : a review. *J. Ind. Eng. Chem.* **2016**, *37*, 1–13.

(20)   Gambo, Y.; Jalil, A. A.; Triwahyono, S.; Abdulrasheed, A. A. Recent advances and future prospect in catalysts for oxidative coupling of methane to ethylene : A Review. *J. Ind. Eng. Chem.* **2018**, *59*, 218–229.

(21)   Lane, G. S.; Miró, E. E.; Wolf, E. E. Methane oxidative coupling: II. A study of Lithium-Titania-catalyzed reactions of methane. *J. Catal.* **1989**, *119*, 161–178.

(22)   Deboy, J. M.; Hicks, R. F. Kinetics of the Oxidative Coupling of Methane over 1 Wt%Sr/La$_2$O$_3$. *J. Catal.* **1988**, *113*, 517–524.

(23)   Habibpoor, H.; Taghizadeh, M.; Raouf, F. Oxidative coupling of methane over Li/MgO catalysts prepared by sol-gel and impregnation methods. *Inorg. Nano-Metal Chem.* **2017**, *47*, 1449–1456.

(24)   Kondratenko, E. V.; Schlüter, M.; Baerns, M.; Linke, D.; Holena, M. Developing catalytic materials for the oxidative coupling of methane through statistical analysis of literature data. *Catal. Sci. Technol.* **2015**, *5*, 1668–1677.

(25)   Karakaya, C.; Zhu, H.; Zohour, B.; Senkan, S.; Kee, R. J. Detailed reaction mechanisms for the oxidative coupling of methane over La$_2$O$_3$/CeO$_2$ nanofiber fabric catalysts. *ChemCatChem* **2017**, *9*, 4538–4551.

(26)   Groppi, G.; Tronconi, E. Design of novel monolith catalyst supports for gas/solid reactions with heat exchange. *Chem. Eng. Sci.* **2000**, *55*, 2161–2171.

(27)   Cybulski, A.; Moulin, J. Monoliths in Heterogeneous Catalysis. *Catal. Rev.* **1994**, *36*, 179–270.

27

(28)   Sollier, B. M.; Gómez, L. E.; Boix, A. V.; Miró, E. E. Oxidative coupling of methane on Sr/La$_2$O$_3$ catalysts: Improving the catalytic performance using cordierite monoliths and ceramic foams as structured substrates. *Appl. Catal. A Gen.* **2017**, *532*, 65–76.

(29)   Sollier, B. M.; Gómez, L. E.; Boix, A. V.; Miró, E. E. Oxidative coupling of methane on cordierite monoliths coated with Sr/La$_2$O$_3$ catalysts. Influence of honeycomb structure and catalyst-cordierite chemical interactions on the catalytic behavior. *Appl. Catal. A Gen.* **2018**, *550*, 113–121.

(30)   Noon, D.; Seubsai, A.; Senkan, S. Oxidative coupling of methane by nanofiber catalysts. *ChemCatChem* **2013**, *5*, 146–149.

(31)   Noon, D.; Zohour, B.; Bae, A.; Seubsai, A.; Senkan, S. Effects of Ir-doping on the transition from oxidative coupling to partial oxidation of methane in La$_2$O$_3$-CeO$_2$ nanofiber catalysts: Spatial concentration and temperature profiles. *RSC Adv.* **2017**, *7*, 26783–26789.

(32)   Song, J.; Sun, Y.; Ba, R.; Huang, S.; Zhao, Y.; Zhang, J.; Sun, Y.; Zhu, Y. Monodisperse Sr-La$_2$O$_3$ hybrid nanofibers for oxidative coupling of methane to synthesize C2 hydrocarbons. *Nanoscale* **2015**, *7*, 2260–2264.

(33)   Xu, Y.; Bao, X.; Lin, L. Direct conversion of methane under nonoxidative conditions. *J. Catal.* **2003**, *216*, 386–395.

(34)   Sinev, M. Y.; Fattakhova, Z. T.; Lomonosov, V. I.; Gordienko, Y. A. Kinetics of oxidative coupling of methane: bridging the gap between comprehension and

28

description. *J. Nat. Gas Chem.* **2009**, *18*, 273–287.

(35) Lacoste, A. M.; Tiscornia, I. S.; Boix, A. V. CO preferential oxidation on cordierite monoliths coated with CuO-CeO$_2$/SBA-15 catalysts. Further insights into the physico-chemical aspects of the catalytic behavior. *Int. J. Hydrogen Energy* **2018**, *43*, 14238–14251.

(36) Dedov, A. G.; Loktev, A. S.; Moiseev, I. I.; Aboukais, A.; Lamonier, J. F.; Filimonov, I. N. Oxidative coupling of methane catalyzed by rare earth oxides: Unexpected synergistic effect of the oxide mixtures. *Appl. Catal. A Gen.* **2003**, *245*, 209–220.

(37) Cao, X.; Vassen, R.; Fischer, W.; Tietz, F.; Jungen, W.; Stöver, D. Lanthanum-Cerium Oxide as a thermal barrier-coating material for high-temperature applications. *Adv. Mater.* **2003**, *15*, 1438–1442.

(38) Iida, H.; Fujiyama, A.; Igarashi, A.; Okumura, K. Steam reforming of toluene over Ru/SrCO$_3$-Al$_2$O$_3$ catalysts. *Fuel Process. Technol.* **2017**, *168*, 50–57.

(39) Faroldi, B. M.; Lombardo, E. A.; Cornaglia, L. M. Surface properties and catalytic behavior of Ru supported on composite La$_2$O$_3$-SiO$_2$ oxides. *Appl. Catal. A Gen.* **2009**, *369*, 15–26.

(40) Gallaher, G.; Goodwin, J.; Huang, C.-S.; Houalla, M. XPS and reaction investigation of alkali promotion of Rh/La$_2$O$_3$. *J. Catal.* **1993**, *140*, 453–463.

(41) Sunding, M. F.; Hadidi, K.; Diplas, S.; Løvvik, O. M.; Norby, T. E.; Gunnæs, A. E. XPS characterisation of in situ treated lanthanum oxide and hydroxide using tailored

29

charge referencing and peak fitting procedures. *J. Electron Spectros. Relat. Phenomena* **2011**, *184*, 399–409.

(42) Paparazzo, E. XPS Studies of damage induced by X-Ray irradiation on CeO_2 surfaces. *Surf. Sci.* **1990**, *234*, L253–L258.

(43) Islam, M. S.; Ilett, D. J.; Parker, S. C. Surface structures and oxygen hole formation on the La_2O_3 catalyst. A computer simulation study. *J. Phys. Chem.* **1994**, *98*, 9637–9641.

(44) Ferreira, V. J.; Tavares, P.; Figueiredo, J. L.; Faria, J. L. Ce-doped La_2O_3 based catalyst for the oxidative coupling of methane. *Catal. Commun.* **2013**, *42*, 50–53.

(45) Bukhtiyarova, M. V.; Ivanova, A. S.; Plyasova, L. M.; Litvak, G. S.; Rogov, V. A.; Kaichev, V. V.; Slavinskaya, E. M.; Kuznetsov, P. A.; Polukhina, I. A. Selective catalytic reduction of nitrogen oxide by ammonia on Mn(Fe)-substituted Sr(La) aluminates. *Appl. Catal. A Gen.* **2009**, *357*, 193–205.

(46) Shen, V. K.; Siderius, D. W.; Krekelberg, W. P.; Hatch, H. W. NIST Standard Reference Simulation Website, NIST Standard Reference Database Nummber 173. National Institute of Standars and Technology http://doi.org/10.18434/T4M88Q.

(47) Kuyyalil, J.; Newby, D.; Laverock, J.; Yu, Y.; Cetin, D.; Basu, S. N.; Ludwig, K.; Smith, K. E. Vacancy assisted SrO formation on $La_{0.8}Sr_{0.2}Co_{0.2}Fe_{0.8}O_{3-\delta}$ surfaces - A synchrotron photoemission study. *Surf. Sci.* **2015**, *642*, 33–38.

(48) Cong, L.; Zhao, Y.; Li, S.; Sun, Y. Sr-doping effects on La_2O_3 catalyst for oxidative coupling of methane. *Chinese J. Catal.* **2017**, *38*, 899–907.

30

(49)   Choudhary, V. R.; Mulla, S. A. R.; Rane, V. H. Oxidative coupling of methane and oxidative dehydrogenation of ethane over strontium-promoted rare earth oxide catalysts. *J. Chem. Technol. Biotechnol.* **1998**, *71*, 167–172.

(50)   González-Cortés, S. L.; Orozco, J.; Fontal, B. Oxidative transformation of methane on 1.5 Mol % Sr^{2+}/La_2O_3 -supported nickel catalysts. *Appl. Catal. A Gen.* **2001**, *213*, 259–271.

(51)   Mestl, G.; Knozinger, H.; Lunsford, J. H. High temperature in situ Raman spectroscopy of working oxidative coupling catalysts. *Ber. Bunsenges Phys. Chem.* **1993**, *97*, 319–321.

(52)   Stefov, V.; Abdija, Z.; Najdoski, M.; Koleva, V.; Petruševski, V. M.; Runčevski, T.; Dinnebier, R. E.; Šoptrajanov, B. Infrared and Raman spectra of magnesium ammonium phosphate hexahydrate (Struvite) and its isomorphous analogues. IX: Spectra of protiated and partially deuterated cubic magnesium caesium phosphate hexahydrate. *Vib. Spectrosc.* **2013**, *68*, 122–128.

(53)   Thybaut, J. W.; Sun, J.; Olivier, L.; Van Veen, A. C.; Mirodatos, C.; Marin, G. B. Catalyst design based on microkinetic models: Oxidative coupling of methane. *Catal. Today* **2011**, *159*, 29–36.

(54)   Takanabe, K.; Iglesia, E. Rate and selectivity enhancements mediated by OH radicals in the oxidative coupling of methane catalyzed by $Mn/Na_2WO_4/SiO_2$. *Angew. Chemie - Int. Ed.* **2008**, *47*, 7689–7693.

(55)   Reyes, S.; Iglesia, E.; Kelkar, C. P. Kinetic-transport models of bimodal reaction

sequences- I. Homogeneous and heterogeneous pathways in oxidative coupling of methane. *Chem. Eng. Sci.* **1993**, *48*, 2643–2661.

(56) Chen, Q.; Couwenberg, P. M.; Marin, G. B. Effect of pressure on the oxidative coupling of methane in the absence of catalyst. *AIChE J.* **1994**, *40*, 521–535.

(57) Farsi, A.; Mansouri, S. S. Influence of nanocatalyst on oxidative coupling, steam and dry reforming of methane: A short review. *Arab. J. Chem.* **2016**, *9*, S28–S34.

(58) Liu, Z.; Ho Li, J. P.; Vovk, E.; Zhu, Y.; Li, S.; Wang, S.; Van Bavel, A. P.; Yang, Y. Online kinetics study of oxidative coupling of methane over La_2O_3 for methane activation: What Is behind the distinguished light-off temperatures? *ACS Catal.* **2018**, *8* (12), 11761–11772.

(59) Othman, N. H.; Wu, Z.; Li, K. An oxygen permeable membrane microreactor with an in-situ deposited $Bi_{1.5}Y_{0.3}Sm_{0.2}O_{3-\delta}$ catalyst for oxidative coupling of Methane. *J. Memb. Sci.* **2015**, *488*, 182–193.

32
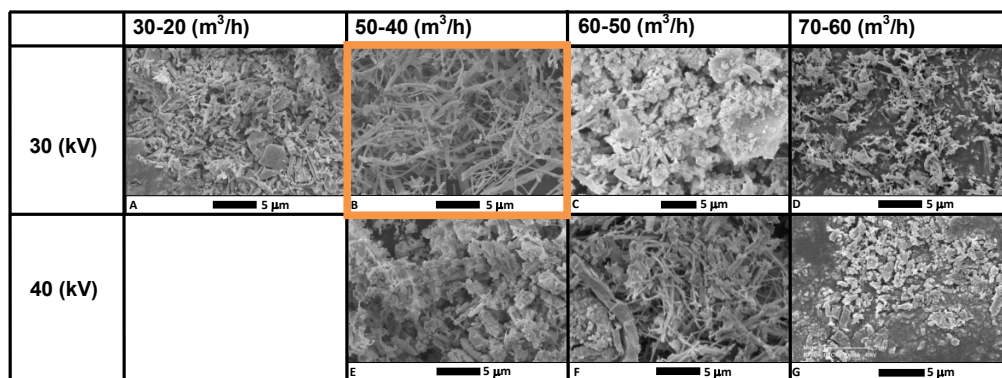
Figure 1. LaCe3 SEM micrographs of different samples (before calcination) obtained by diverse machine parameters: air flows and applied voltages.
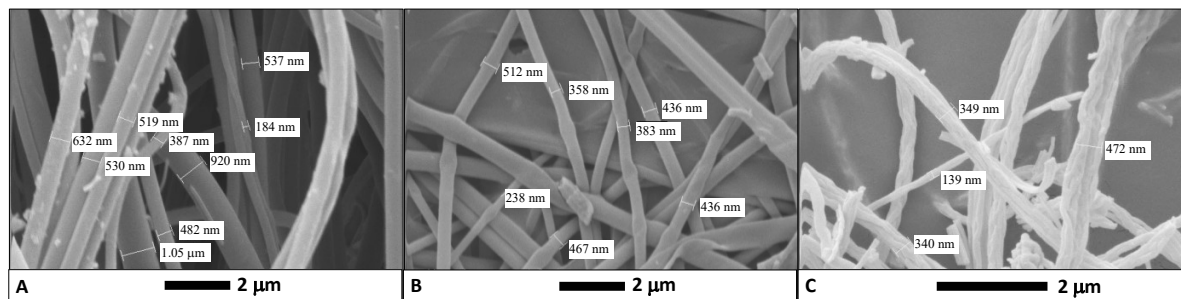
Figure 2. SEM micrographs of: (A) PVP nanofibers. (B) LaCe0.1@PVP nanofibers (before calcination) (C) LaCe0.1 nanofibers (after calcination at 625 °C).
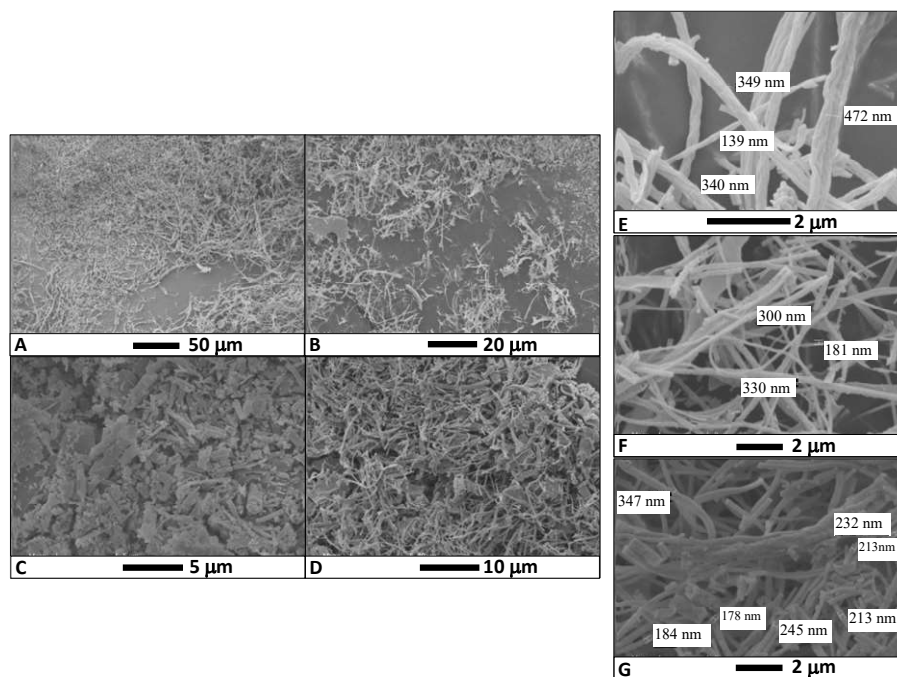
Figure 3. SEM micrographs of LaCe nanofibers (after calcination at 625 °C) with different compositions. (A) and (E) LaCe0.1, (B) and (F) LaCe0.2, (C) LaCe1, and (D) and (G) LaCe3.
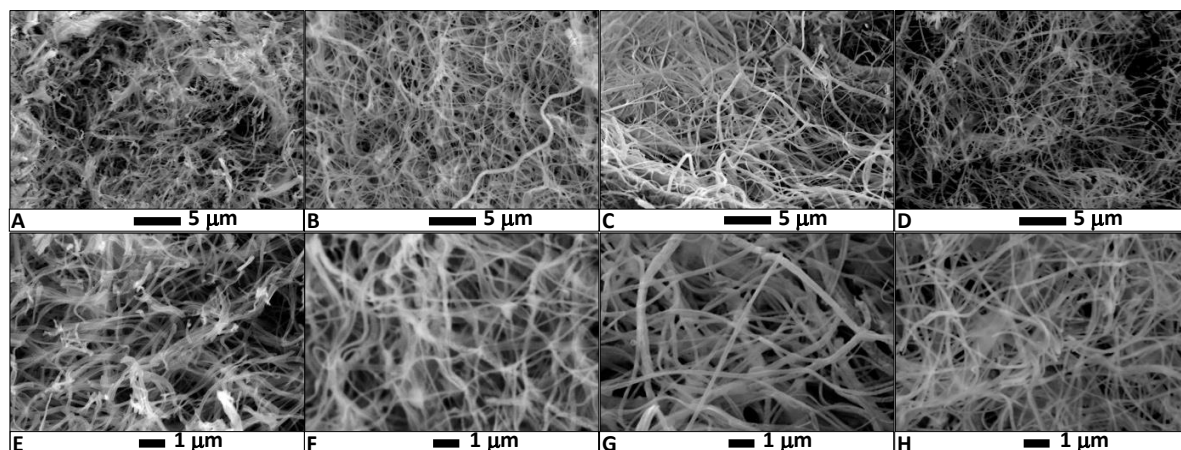
Figure 4. SEM micrographs of SrLaCe nanofibers (after calcination at 625 °C) with different compositions. (A) and (E) SrLaCe0.1, (B) and (F) SrLaCe0.2, (C) and (G) SrLaCe1, and (D) and (H) SrLaCe3.
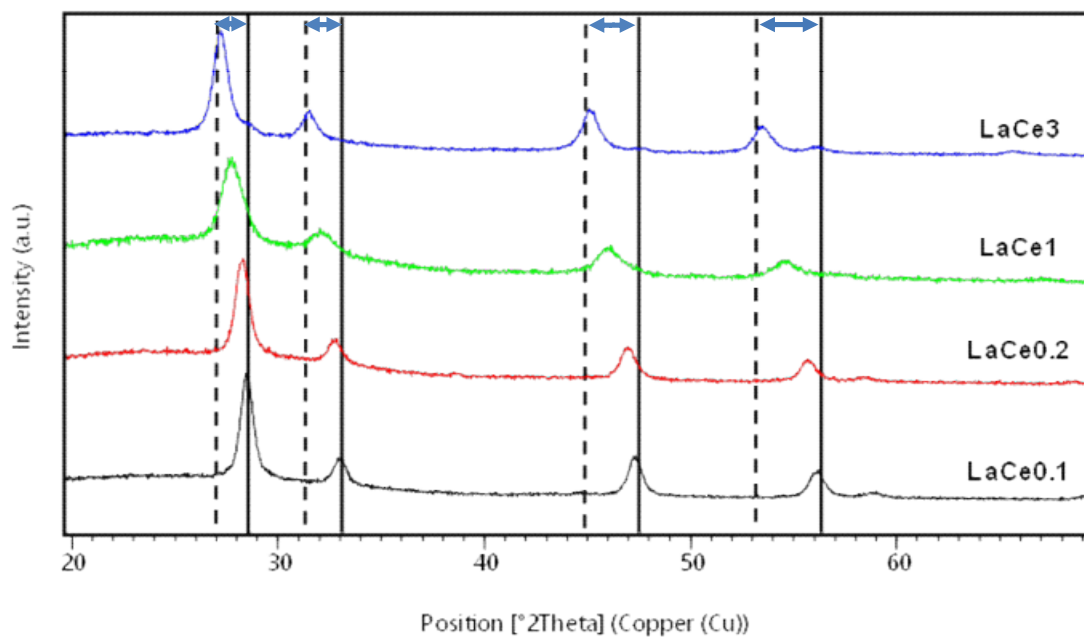
Figure 5. XRD patterns of LaCe0.1, LaCe0.2, LaCe1 and LaCe3 nanofibers: full lines indicate the XRD peak positions of cubic CeO_2 (ICDD card 00-034-0394), dot lines those of La_2O_3 (ICDD card 03-065-3185) and ↔ peak position possibilities of solid solutions $La_xCe_yO_z$.
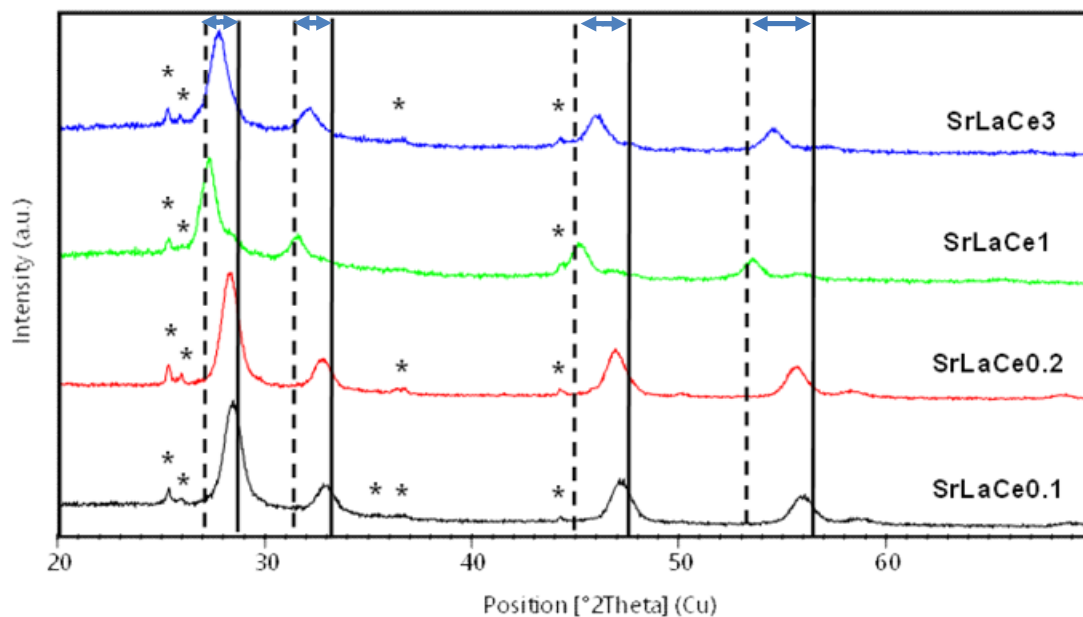
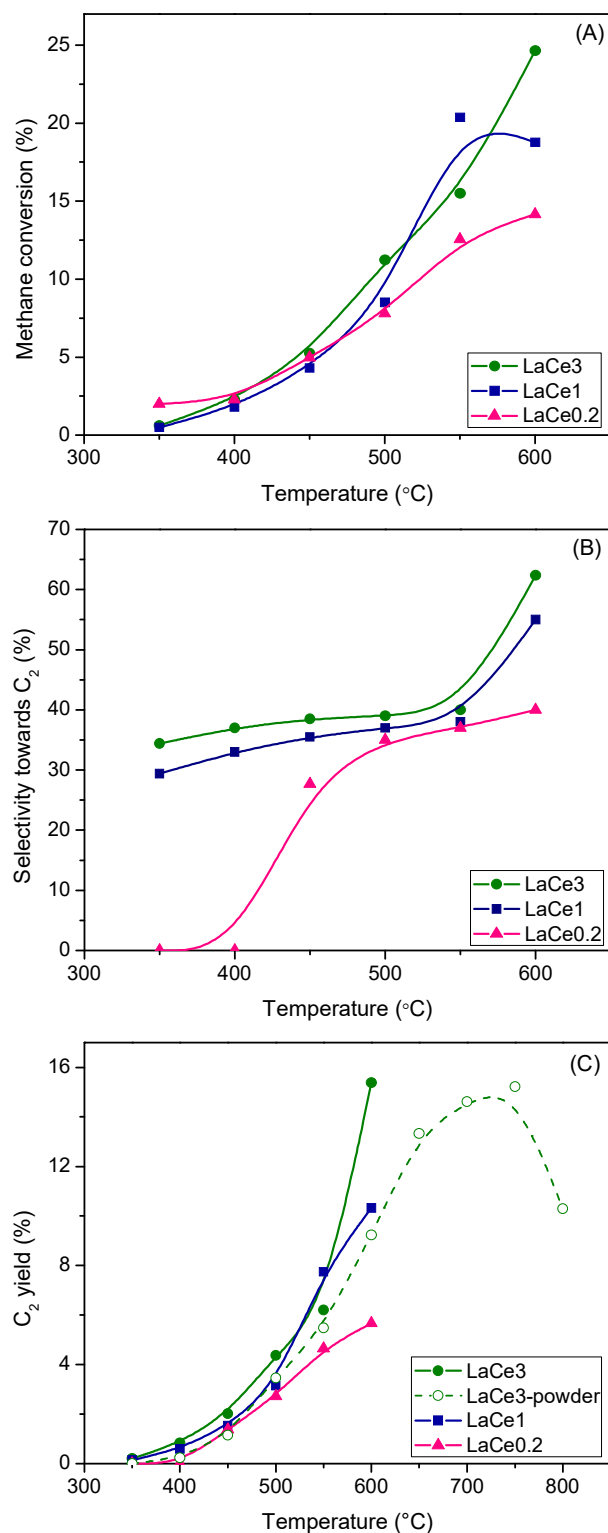**Figure 6.** XRD patterns of SrLaCe0.1, SrLaCe0.2, SrLaCe1 and SrLaCe3 nanofibers: full lines indicate the XRD peak positions of cubic CeO_2 (ICDD card 00-034-0394), dot lines those of La_2O_3 (ICDD card 03-065-3185), * those of $SrCO_3$ and ↔ peak position possibilities of solid solutions $La_xCe_yO_z$.

.
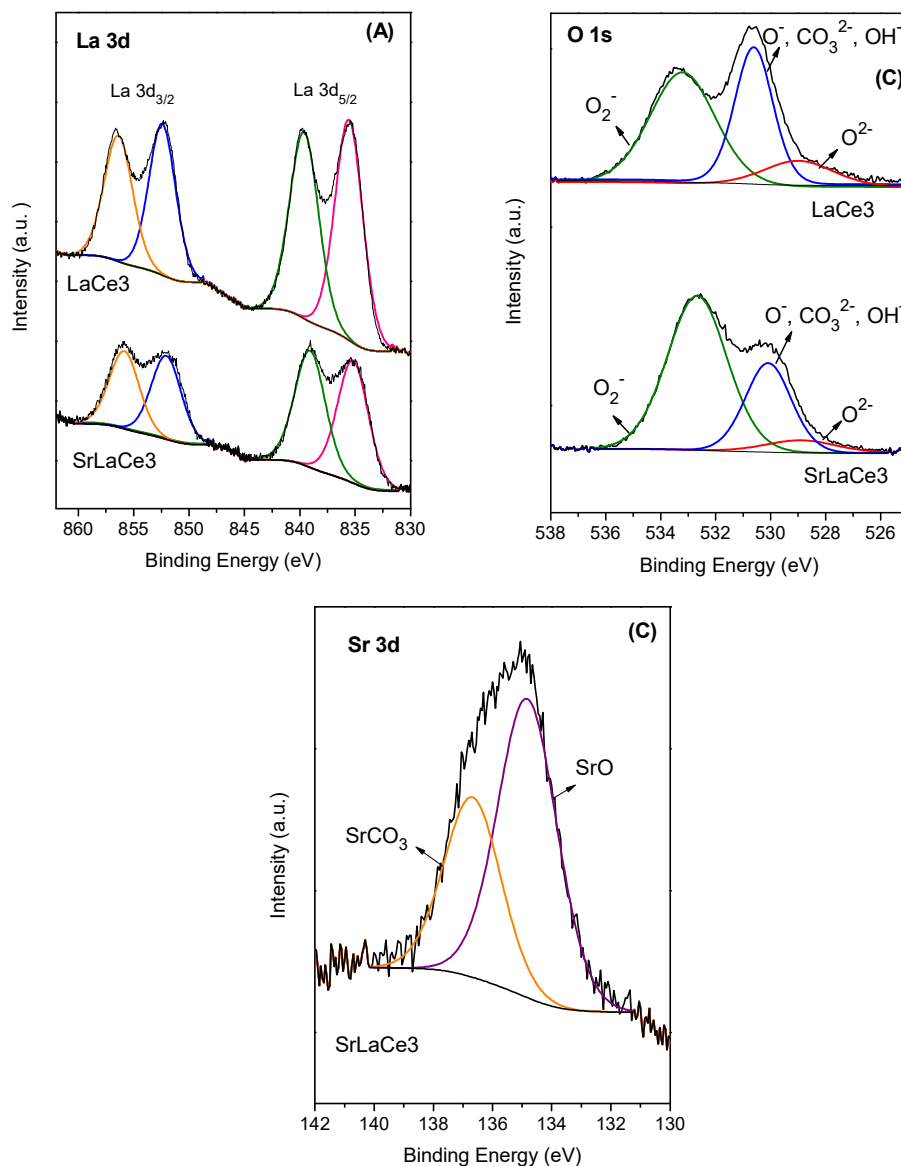
Figure 7. XPS results from SrLaCe3 and LaCe3 of: (A) La 3d, (B) O 1s and (C) Sr 3d regions.

Figure 8. Catalytic behaviour of LaCe nanofibers: (A) Methane conversion, (B) selectivity towards C2 and (C) C2 yield. Reaction conditions: W/F=0.166 mg cm^{-3} h, Flow composition: 60 vol.% CH$_4$, 12 vol.% O$_2$ and 28 % vol. He.
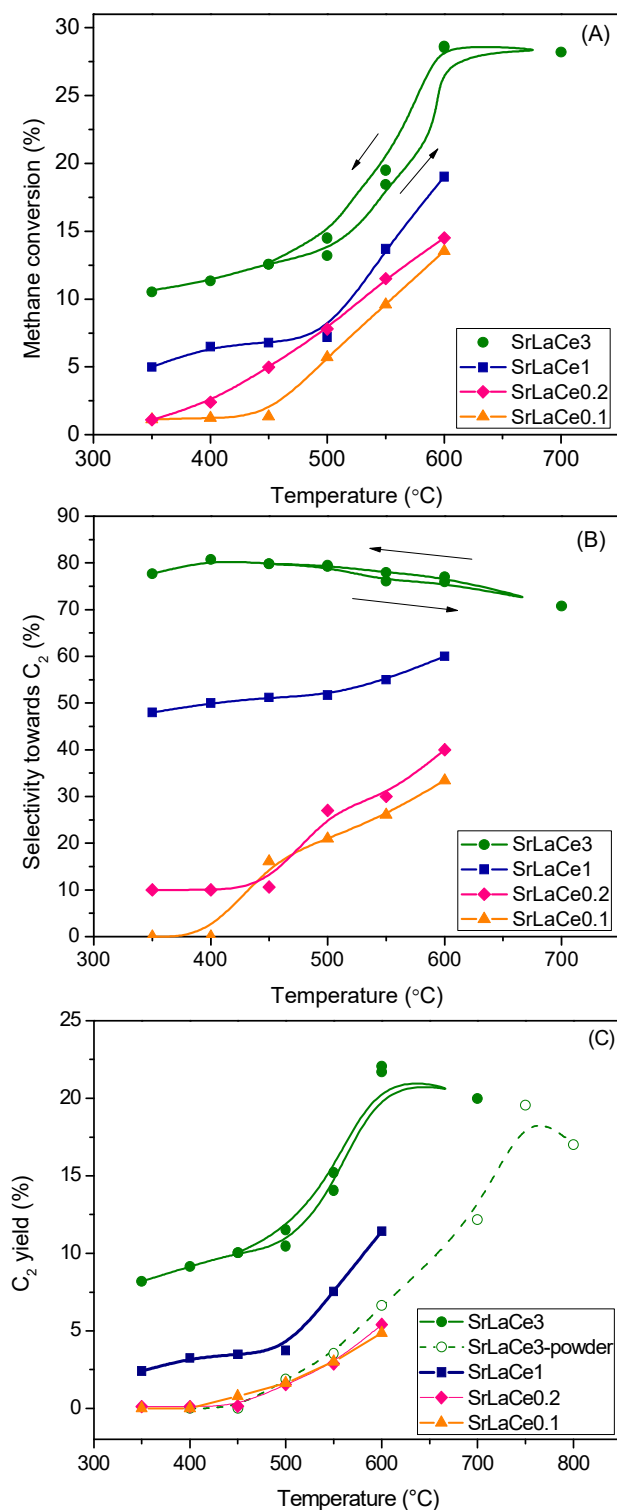
Figure 9. Catalytic behaviour of SrLaCe nanofibers: (A) Methane conversion, (B) selectivity towards C_2 and (C) C_2 yield. Reaction conditions: W/F=0.166 mg cm^{-3} h, Flow composition: 60 vol.% CH_4, 12 vol.% O_2 and 28 % vol. He.

Table 1. Nomenclature of different nanofibers. Theoretical values of sample compositions and XRD identification.

	Ce (wt. %)	La (wt. %)	Sr (wt. %)	La/Ce	Identified phases	ICDD reference cards
LaCe0.1	90	10	-	0.11	Near CeO_2	Near 00-034-0394
LaCe0.2	80	20	-	0.25	$La_{0.2}Ce_{0.8}O_{1.9}$	04-016-6693
LaCe1	50	50	-	1	$La_{0.5}Ce_{0.5}O_2$	04-006-3412
LaCe3	25	75	-	3	No card available but near La_2O_3 + CeO_2	Near 03-065-3185 00-034-0394
SrLaCe0.1	85.7	9.3	5	0.11	$Sr_{0.06}La_{0.03}Ce_{0.91}O_{1.925}$ or $La_{0.05}Ce_{0.95}O_{1.975}$ or $La_{0.1}Ce_{0.9}O_{1.95}$ or $La_{0.15}Ce_{0.85}O_{1.925}$ +$SrCO_3$	04-021-0597 01-080-3723 01-080-3724 04-019-5520 01-084-1778
SrLaCe0.2	76.2	19	5	0.25	Same pattern than LaCe0.2 $(La_{0.2}Ce_{0.8}O_{1.9})$ +$SrCO_3$	04-016-6693 01-084-1778
SrLaCe1	47.6	47.6	5	1	Same phase than LaCe3 + $La_{0.2}Ce_{0.8}O_{1.9}$ +$SrCO_3$	Near 03-065-3185 04-016-6693 01-084-1778
SrLaCe3	23.8	71.4	5	3	Same pattern than LaCe1 $(La_{0.5}Ce_{0.5}O_2)$ +$SrCO_3$	04-018-7404 01-084-1778

Table 2. Atomic concentration of SrLaCe nanofibers obtained by EDX technique.

Catalytic	Atomic concentration (%)				
fibers	Sr	La	Ce	O	C
SrLaCe0.1	4.7	1.9	16.0	57.2	20.2
SrLaCe0.2	4.7	4.9	18.6	48.2	23.6
SrLaCe1	4.5	8.7	8.0	60.4	18.4
SrLaCe3	4.6	18.5	5.8	47.9	23.2

Table 3. XPS analysis results.

Catalytic	Binding Energy (eV)					
fibers	La 3d$_{5/2}$	La 3d$_{3/2}$	Ce 3d$_{5/2}$	Ce 3d$_{3/2}$	O1s	Sr3d
LaCe3	835.6	852.4	882.9	901.0	529.1/8.9 [a]	
	839.6[b]	856.4[b]	888.4	907.6	530.6/44.8	
			898.1	916.5	533.2/46.3	
SrLaCe3	835.3	852.1	882.5	901.0	528.9/14.7	134.8/63.6[a]
	839.1[b]	855.9[b]	888.8	907.1	530.1/21.0	136.6/36.4
			898.5	916.5	532.8/64.3	

[a] Percentage fraction of each component.

[b] Satellite peak

1
2
3
4
5
6
7
8
9
10
11
12
13
14
15
16
17
18
19
20
21
22
23
24
25
26
27
28
29
30
31
32
33
34
35
36
37
38
39
40
41
42
43
44
45
46
47
48
49
50
51
52
53
54
55
56
57
58
59
60

Table 4. Concentration of constituent elements on the nanofibers surface.

Fibers	Surface atomic concentration (%) from XPS				La/Ce
	Sr	La	Ce	O	
LaCe3	-	21.6	4.7	73.4	4.6
SrLaCe3	3.6	14.9	3.5	78.0	4.2

45

Abstract Graphics